SCIENTIFIC REPORTS

OPEN

All Sequential Dip-Coating Processed Perovskite Layers from an Aqueous Lead Precursor for High Efficiency Perovskite Solar Cells

Received: 22 November 2017
Accepted: 16 January 2018
Published online: 01 February 2018

Muhammad Adnan[1] & Jae Kwan Lee[1,2]

A novel, sequential method of dip-coating a ZnO covered mesoporous TiO_2 electrode was performed using a non-halide lead precursor in an aqueous system to form a nanoscale perovskite film. The introduction of a ZnO interfacial layer induced significant adsorption in the non-halide lead precursor system. An efficient successive solid-state ion exchange and reaction process improved the morphology, crystallinity, and stability of perovskite solar cells. Improved surface coverage was achieved using successive ionic layer adsorption and reaction processes. When all sequential dipping conditions were controlled, a notable power conversion efficiency of 12.41% under standard conditions (AM 1.5, 100 mW·cm^{-2}) was achieved for the perovskite solar cells fabricated from an aqueous non-halide lead precursor solution without spin-casting, which is an environmentally benign and low-cost manufacturing processes.

Recently, organic-inorganic lead halide perovskite solar cells (PrSCs) have received significant attention because of their excellent breakthrough power conversion efficiencies (PCEs) of ~21%, making them potential surrogates for conventional silicon-based solar cells[1–10]. Most organometallic halides, particularly alkylammonium lead halides, (RNH_3) PbX_3 (R = alkyl, X = Cl, Br, I), are direct-band-gap materials that are primarily used as hybrid organic-inorganic perovskite cores with exceptional electron and hole conduction and photosensitizer performance[11,12]. The coverage, crystallinity, and uniformity of perovskite materials on its substrate are essential for boosting the PCEs of the fabricated devices. Hence, an significant attention has been devoted to the development of efficient fabrication methods for perovskite material layers in PrSCs. A myriad of strategies have been proposed to improve the PCEs with lead sources of PbX_2, $Pb(OAc)_2$, or $Pb(NO_3)_2$[13,14]. Proposed methods include: (1) the sequential deposition from spin-casting of a lead source followed by reaction with an alkylammonium halide, such as methylammonium iodide (CH_3NH_3I, MAI), by dipping in solution, spin-casting, or vacuum deposition[2–15]; and (2) the direct spin-casting of a perovskite precursor solution combined with, adduct, thermal annealing, interfacial engineering, solvent-engineering, or processing additive treatment[16–25]. These methods have provided satisfactorily high PCEs; however, the fabricated PrSCs frequently possess small active areas and suffer from substrate size limitation during spin-casting. Thus, it is challenging, yet essential for commercial applications, to develop inexpensive manufacturing processes that facilitate large area perovskite film formation, via efficient routes including dip-coating, doctor-blade methods, and inkjet or roll-to-roll printing[1–26].

Most studies have used toxic high-polarity aprotic organic solvents, such as dimethylformamide, due to the poor solubility of the lead precursors. Non-halide lead precursors, such as $Pb(OAc)_2$ and $Pb(NO_3)_2$, have recently attracted interest because of their compatibility with non-toxic solvents such as water[3]. Heish *et al.* reported a $MAPbI_3$ perovskite film fabricated by sequential deposition[27]. An aqueous $Pb(NO_3)_2$ solution was spin-cast onto UV/ozone-pretreated mesoporous TiO_2 (m-TiO_2)/compact TiO_2 (c-TiO_2) layers, followed by a two-step reaction in the MAI solution. The first step involved PbI_2 formation via ion-exchange reaction between $Pb(NO_3)_2$ and MAI and the second involved $MAPbI_3$ perovskite formation from PbI_2 and MAI. Although the $Pb(NO_3)_2$ film was uniformly spin-cast onto the m-TiO_2 layer, the morphology and coverage of the PbI_2 film formed in the first step was significantly impaired. This impairment was caused by the structural change induced by the difference

[1]Department of Chemistry, Graduate School, Chosun University, Gwangju, 501-759, Republic of Korea. [2]Department of Chemistry Education/Carbon Materials, Chosun University, Gwangju, 501-759, Republic of Korea. Correspondence and requests for materials should be addressed to J.K.L. (email: chemedujk@chosun.ac.kr)

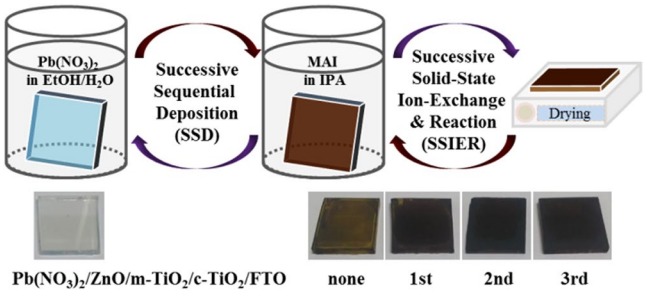

Figure 1. Schematic description of the preparation of $MAPbI_3$ perovskite films using sequential dipping of ZnO covered m-TiO_2/c-TiO_2/FTO substrates in aqueous $Pb(NO_3)_2$ and MAI solutions. Included are pictures of the as-prepared electrodes after a designated number of SSIER repetitions followed by annealing for 10 min at room temperature.

in ionic radii between I^- and NO_3^-. In the following step, well-defined morphology and coverage of the $MAPbI_3$ perovskite film on the substrate was not achieved compared to those fabricated by spin-cast PbI_2 films. To overcome these challenges, we have been interested in developing novel and efficient approaches for perovskite film formation. Preparation from aqueous non-halide lead precursor solutions using non-spin-casting methods is a proposed environmentally benign and low-cost manufacturing processes for large area devices. Recently, ionic layer adsorption, followed by reaction of $Pb(NO_3)_2$ on a ZnO heterostructure, in aqueous solution has been reported as an attractive approach for the formation of PbS quantum dot layers[28,29]. Thus, we have attempted to form an efficient $MAPbI_3$ perovskite film by the ionic layer adsorption of aqueous $Pb(NO_3)_2$ by introducing a ZnO interfacial layer on top of a m-TiO_2 film, followed by reaction with MAI. We speculate that this successive sequential deposition (SSD) via dip-coating might facilitate the production of large area perovskite films using non-halide lead precursors in aqueous solution.

In this study, we demonstrate a facile, cost-effective, and environmentally benign approach to prepare efficient perovskite films by simple dip-coating deposition. This was demonstrated by sequentially dipping of a ZnO-covered m-TiO_2 film in an aqueous lead precursor solution and then the MAI solution. This process contrasts with conventional spin-casting approaches that require harsh organic solvents.

Herein, we found that the ZnO interfacial layer quickly induces significant adsorption of $Pb(NO_3)_2$ from the aqueous solution. The $MAPbI_3$ perovskite was also formed via $Pb(NO_3)_2$ and PbI_2 undergoes additional ion-exchange reactions with the un-reacted $Pb(NO_3)_2$ even in the solid state, resulting in decomposition to PbI_2. Notably, the successive solid-state ion-exchange and reaction (SSIER) with the $Pb(NO_3)_2$ layer resulted in improved crystallinity, morphology, and coverage as well as stability of the $MAPbI_3$ film compared to materials produced by long-time dipping in MAI solution. Moreover, the perovskite film fabricated with the combined SSD and SSIER techniques exhibited superior crystallinity, morphology, and coverage compared to those made with either approach alone. The PrSCs fabricated by the sequential deposition of a $MAPbI_3$ perovskite layer using an aqueous $Pb(NO_3)_2$ solution exhibited PCEs of 12.41%, which is comparable to films fabricated by spin-casting of halide or non-halide lead precursors. Figure 1 shows a schematic description of the preparation of the $MAPbI_3$ perovskite films by sequentially dipping a ZnO-covered m-TiO_2/c-TiO_2/fluorine-doped tin oxide (FTO) substrate in aqueous $Pb(NO_3)_2$ and MAI solutions.

Results and Discussion

Perovskite film formation. For the formation of perovskites, we first fabricated the Pb layer by dipping the substrate into a $Pb(NO3)_2$ solution. Figure 2(a,c) shows the SEM surface morphologies after ionic layer adsorption of $Pb(NO_3)_2$ on m-TiO_2/c-TiO_2/FTO substrates with and without a ZnO layer. In Fig. 2(b,d) the as-prepared $MAPbI_3$ perovskite layers formed when the ZnO-free and ZnO-coated samples were exposed to the MAI solution can be seen. We chose $Pb(NO_3)_2$ as the non-halide lead precursor because it exhibited better ionic layer adsorption on ZnO surfaces in aqueous solutions (see Fig. S1 in the Supplementary Information). Thin ZnO layer-incorporated m-TiO_2 films were used because they could be readily prepared by spin-casting or spray-coating of the sol-gel precursor solution, followed by annealing at 300 °C (Fig. S2). Interestingly, significant layer adsorption of $Pb(NO_3)_2$ was observed on the surface of the ZnO-coated substrate after the simple dip-coating process in the aqueous $Pb(NO_3)_2$ solution, but negligible layer adsorption on the m-TiO_2 films was observed without the ZnO layer (Fig. 2(a) and (b)).

This unprecedented $Pb(NO_3)_2$ layer adsorption occurred on the ZnO surface within a very short time, which can be tuned by adjusting the lead precursor solution, especially the co-solvent system of H_2O/ethanol. A more uniform adsorption was observed on the hydrophobic ZnO surface compared with the water-only solvent[30,31]. By adsorption can also be changed by tuning the dipping times, as shown in Fig. S3. For $MAPbI_3$ perovskite formation from the reaction with MAI, the $Pb(NO_3)_2$ layer was first deposited by dip-coating in a 0.1 M $Pb(NO_3)_2$ solution, dissolved in H_2O/ethanol (1:1, v/v), for 30 s. As shown in Fig. 1c and d, the transparent $Pb(NO_3)_2$ layers adsorbed on the ZnO layer-coated m-TiO_2 film. These layers rapidly changed to dark brown-colored films upon exposure to the MAI solution, exhibiting a $MAPbI_3$ perovskite film morphology and poor coverage similar to those formed by spin-casting of the $MAPbI_3$ precursor solution without any treatment. However, the transparent $Pb(NO_3)_2$ layers, which adsorbed minimally on the pristine ZnO-free m-TiO_2 film, changed to pale orange-colored films with $MAPbI_3$ perovskite crystal lumps grown sparsely on the substrate.

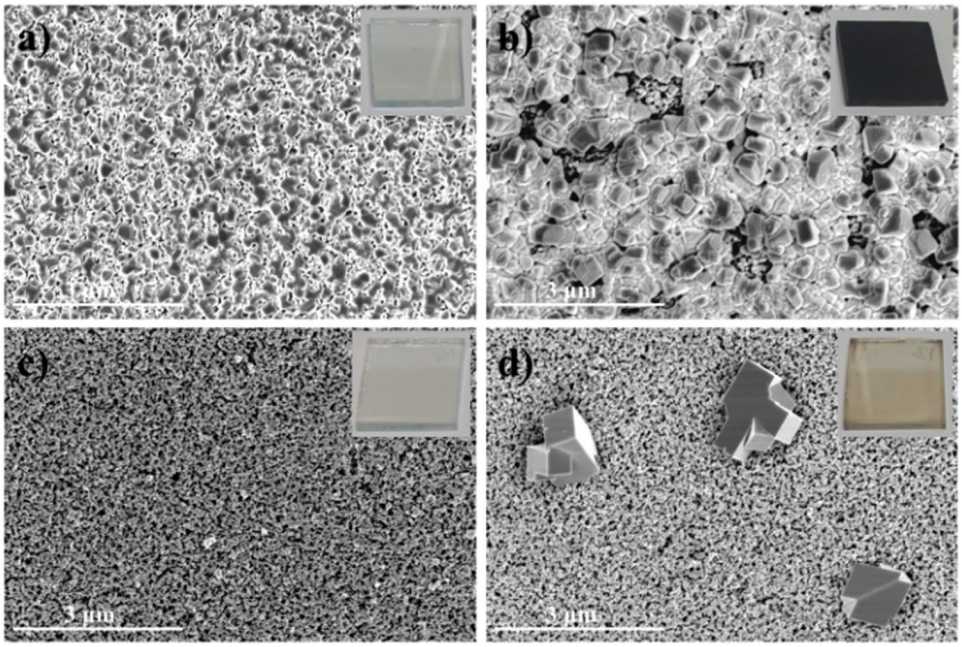

Figure 2. SEM images for surface morphologies from (**a**,**c**) the ionic layer adsorption of $Pb(NO_3)_2$ and (**b**,**d**) the as-prepared $MAPbI_3$ perovskite layers formed after the MAI exposure of the (**a**,**b**) ZnO-coated and (**c**,**d**) ZnO-free m-TiO_2/c-TiO_2/FTO substrates.

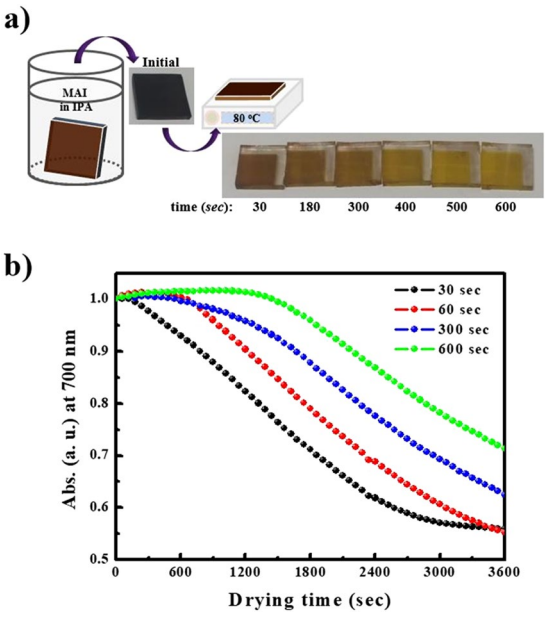

Figure 3. Decomposition (**a**) during solvent drying of a $MAPbI_3$ perovskite film, fabricated by sequential dip-coating deposition with aqueous $Pb(NO_3)_2$ precursor and MAI solutions. The decrease of absorbance (**b**) at 700 nm over 1 h after various MAI solution dipping times (30 (black), 60 (red), 300 (blue), and 600 s (green)).

These results indicate that the sequential approach based on the layer adsorption on ZnO of aqueous $Pb(NO_3)_2$ followed by reaction in a MAI solution facilitates perovskite film formation using inexpensive and simple dip-coating deposition processes. However, the $MAPbI_3$ perovskite film fabricated by this approach rapidly decomposed during solvent drying at 80 °C, even below 20% relative humidity, the change to a yellowish film corresponded to a PbI_2 crystalline morphology.

Decomposition behaviour of perovskite film. Figure 3 shows the decomposition observed during solvent drying of the $MAPbI_3$ perovskite film fabricated by sequential dip-coating deposition. Also shown in Fig. 3b is the decrease of absorbance at 700 nm over 1 h for the $MAPbI_3$ perovskite materials formed with various MAI

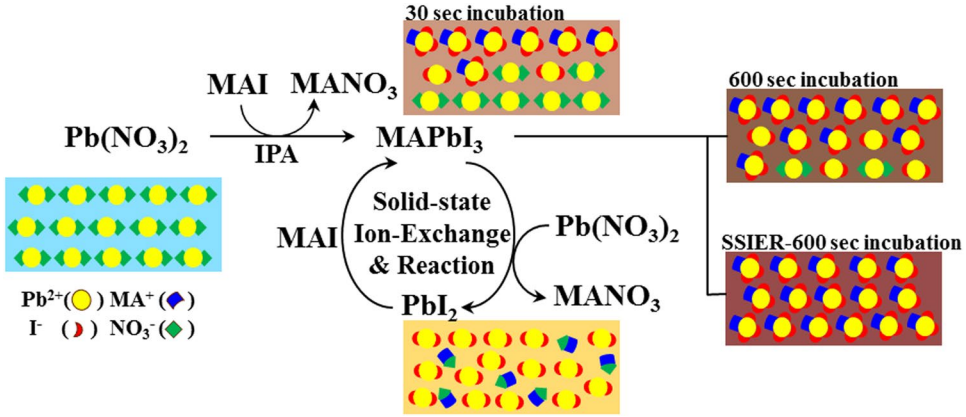

Figure 4. Schematic description of the proposed SSIER approach to $MAPbI_3$ perovskite formation from the as-deposited $Pb(NO_3)_2$ layer and MAI.

solution dipping times (30, 60, 300, and 600 s). As shown in Fig. 3a, film decomposition occurred within a very short time of 30 s and was completed after 10 min of annealing at 80 °C. Decomposition was partially observed even in films fabricated with a long exposure (600 s) to the MAI solution (Fig. 1).

Thus, we investigated the decomposition rate of the films formed with various dipping times by following the decrease in absorbance at 700 nm. Although the as-prepared $MAPbI_3$ perovskite films had a similar dark brown-color upon removal from the MAI solution regardless of the reaction times, the decomposition rates were remarkably affected by the reaction time in the MAI solution (Fig. 3b). This indicates that unreacted $Pb(NO_3)_2$ likely induces the decomposition of the $MAPbI_3$ perovskite crystalline layer, and the degree of unreacted $Pb(NO_3)_2$ should affect the decomposition rates. From these results, we speculate that the $MAPbI_3$ formed from the $Pb(NO_3)_2$ and MAI solutions can participate in ion-exchange reactions between the unreacted $Pb(NO_3)_2$, even in the solid state, resulting in decomposition to PbI_2. Therefore, we developed an efficient approach, denoted as successive solid-state ion-exchange and reaction (SSIER). This method prevents the decomposition of the $MAPbI_3$ perovskite into PbI_2 by the ion-exchange reaction in the solid state between unreacted $Pb(NO_3)_2$ and the as-formed $MAPbI_3$.

Figure 4 shows a schematic description of the proposed mechanism of SSIER for $MAPbI_3$ perovskite formation. Initially, the PbI_2 produced from the reaction of $Pb(NO_3)_2$ and MAI at the solid-liquid interface is converted rapidly into $MAPbI_3$, which undergoes further reactions with MAI. However, the ongoing diffusion of MAI into the film is obstructed by the bulky $MAPbI_3$ perovskite structures formed on the film surface, retarding the reaction rate of $Pb(NO_3)_2$ and MAI. Thus, although the $Pb(NO_3)_2$ layer is exposed to the MAI solution for a long time, unreacted $Pb(NO_3)_2$ likely remains and can induce the decomposition of the $MAPbI_3$ perovskite structure, even in the solid state. Meanwhile, the $Pb(NO_3)_2$ inside the film would be removed, as shown in Fig. 4.

We attempted to efficiently achieve more stable $MAPbI_3$ films without unreacted $Pb(NO_3)_2$ by applying the SSIER process with a exposure time of 30 s to the MAI solution followed by annealing at 80 °C. This represented a single SSIER cycle. No apparent decomposition of the $MAPbI_3$ film was observed after the 3rd SSIER cycle after a total MAI exposure time of 90 s. The $MAPbI_3$ film morphologies formed with and without SSIER repetition were also compared.

Characterization of perovskite film. A specific study regarding the SSIER was successfully performed as shown in Fig. 5. Figure 5a shows the SEM surface morphologies with their corresponding pictures (inset) and Fig. 5b shows XDR patterns for the $MAPbI_3$ perovskite layers fabricated by SSIER repetitions for a total MAI exposure time of 690 s. The correlation between the perovskite conversion and SSIER repetition time is shown in Fig. 5c. These films were annealed at 80 °C for 10 min to completely remove the solvent. We used a $Pb(NO_3)_2$ layer deposited by dip-coating in an aqueous $Pb(NO_3)_2$ solution for a 30 s followed by drying at 120 °C.

As shown in Fig. 5a, even though these $Pb(NO_3)_2$ films were exposed for 690 s to the MAI solution with varied SSIER repetitions and long dipping times, the morphologies of the formed $MAPbI_3$ film was significantly affected by the number of SSIER cycles. The decomposition of the $MAPbI_3$ films was partially observed after the first cycle, as well as the films fabricated with no SSIER cycles. The $MAPbI_3$ films formed after 2 SSIER cycles exhibited better stability (inset of Fig. 5a) compared to the 0 and 1 cycle films. Moreover, with more SSIER cycles, the surface coverage and crystallinity of the $MAPbI_3$ perovskite films improved, as shown by the SEM surface morphologies and XRD patterns (Fig. 5a and b). Also, based on the XRD patterns, the conversion of $MAPbI_3$ (C_{MAPbI3}) could be qualitatively defined using the peak intensities of PbI_2 and $MAPbI_3$ at $2\theta = 12.7°$ and 14.2°, respectively[7,31,32].

$$C_{MAPbI3} = I_{12.7°}/(I_{12.7°} + I_{14.2°}) \quad (1)$$

As shown in Fig. 5c, a greater number of SSIER repetitions gave higher conversion values for $MAPbI_3$ perovskite generated from PbI_2. These parameters are closely related by to the PbI_2 derived from the ion-exchange reaction with the $MAPbI_3$ perovskite and the unreacted $Pb(NO_3)_2$ in the solid state. It should be noted that the SSIER approach can provide superior stability as well as a better surface coverage and crystallinity of $MAPbI_3$ perovskite films.

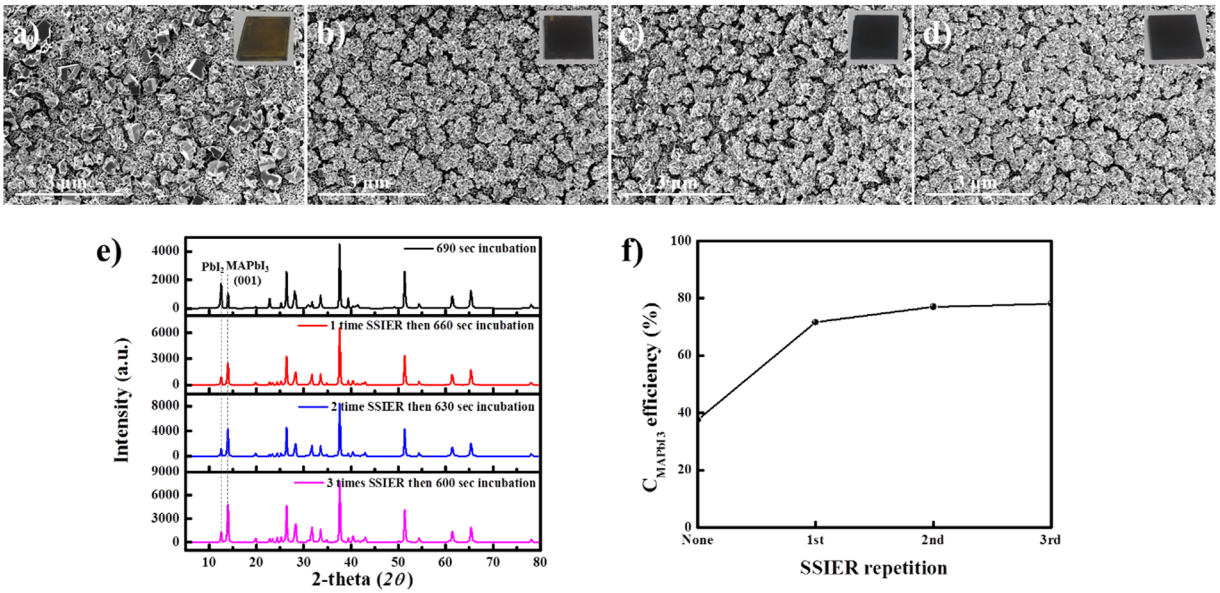

Figure 5. (**a**–**d**) The SEM surface morphologies with the corresponding pictures (inset) and (**e**) XDR patterns of the $MAPbI_3$ perovskite layers fabricated by SSIER repetitions for a total MAI exposure time of 690 s. (**f**) The correlation between the perovskite conversion and SSIER repetition time.

Although the SSIER repetition showed a well-developed surface coverage, crystallinity, and stability, it resulted in rather sparse surface coverage on the ZnO/m-TiO_2/c-TiO_2/FTO substrates, as shown in Fig. 5a. Inadequate surface coverage can lead to interfacial recombination between metal oxides and hole transporting materials (HTMs), resulting in the poor performance of the PrSC devices. Thus, a more complete surface coverage with the $MAPbI_3$ perovskite films was attempted by introducing the SSD process in addition to the SSIER approach. Since the SSD process has been used for the step-by-step growth of nanoscale quantum dot layers[9], we expected that the $MAPbI_3$ perovskite deposited by SSD repetition could effectively improve the sparse coverage. In this study, the $Pb(NO_3)_2$ layer was deposited by dip-coating in an aqueous solution for 30 s, followed by drying at 120 °C. Then, it was exposed to the MAI solution for a 30 s to produce the $MAPbI_3$ perovskite, followed by annealing at 80 °C. The above procedure describes a single SSD cycle.

Meanwhile, the surface morphologies of the $MAPbI_3$ perovskite layers made by conventional SSD processes by (a–c) ionic layer adsorption of $Pb(NO_3)_2$ from aqueous solution followed by (d–f) the reaction in MAI solution, shown in Fig. 6. The XRD patterns of the $MAPbI_3$ perovskite layers and the correlation between perovskite conversion and SSD repetition time are also shown in Fig. 6g.

As shown in Fig. 6a–c, when the as-formed $MAPbI_3$ electrodes were exposed to aqueous $Pb(NO_3)_2$ solution, the water dissolved and removed the MAI from the $MAPbI_3$ perovskite structure, leaving PbI_2. A new layer of $Pb(NO_3)_2$ was simultaneously adsorbed on the surface of the ZnO/m-TiO_2/c-TiO_2/FTO substrate. Interestingly, more platelet structures of PbI_2 were observed with increasing numbers of SSD cycles. In addition, a small increase in adsorption layer thickness was observed with the addition of $Pb(NO_3)_2$, even when comparing films after many SSD repetitions to those with only the first adsorption layer. This indicates that the additional $Pb(NO_3)_2$ is mainly adsorbed on the exposed ZnO/m-TiO_2/c-TiO_2/FTO because of the hydrophobicity of the PbI_2 layers formed during the MAI removal in aqueous solution.

The $MAPbI_3$ films were prepared via 3 SSIER cycles followed by a final incubation for 600 s in the MAI solution after each cycle of $Pb(NO_3)_2$ ionic layer adsorption (Fig. S4). As shown in Fig. 6(d–f), higher numbers of SSD repetitions results in superior surface coverage of the $MAPbI_3$ perovskite films on the substrate. After the 3rd SSD cycle, there were fewer pin-holes in the $MAPbI_3$ perovskite films compared to those fabricated with two or fewer cycles. It should be noted that the $MAPbI_3$ perovskite deposited by SSD repetition can effectively improve the sparse coverage on the ZnO/m-TiO_2/c-TiO_2/FTO. Regarding the XRD patterns, the conversion of $MAPbI_3$ (C_{MAPbI3}) is independent of the 1st to 3rd SSD processes, but significantly decreased after the 4th SSD repetition, as shown in Fig. 6h. These results indicate that the crystallinity of the $MAPbI_3$ perovskite films is mainly affected by the SSIER process, not the SSD process. Furthermore, SSIER might not be effective for perovskite crystal growth after the 4th SSD repetition.

Photovoltaic performance of device fabricated with all sequential dip-coating processed perovskite film. Figure 7a shows the current–voltage (J–V) curves under AM 1.5 irradiation (100 $mW{\cdot}cm^{-1}$) for PrSCs based on $MAPbI_3$ perovskite layers fabricated by a designated number of SSD repetitions followed by three SSIER cycles, with a final incubation for 600 s in the MAI solution. Additionally, the hysteresis behaviors of PrSCs fabricated under the optimized conditions (3 SSD and 3 SSIER cycles, 600 s MAI incubation) are shown in Fig. 7b. The PrSCs were fabricated with an n-i-p structure of FTO/c-TiO_2/m-TiO_2/ZnO/$MAPbI_3$/HTM/MoO_3/Ag. The conductivity of 2,2′,7,7′-tetrakis(*N*,*N*-di-4-methoxyphenylamino)-9,9′-spirobifluorene (spiro-MeOTAD) and

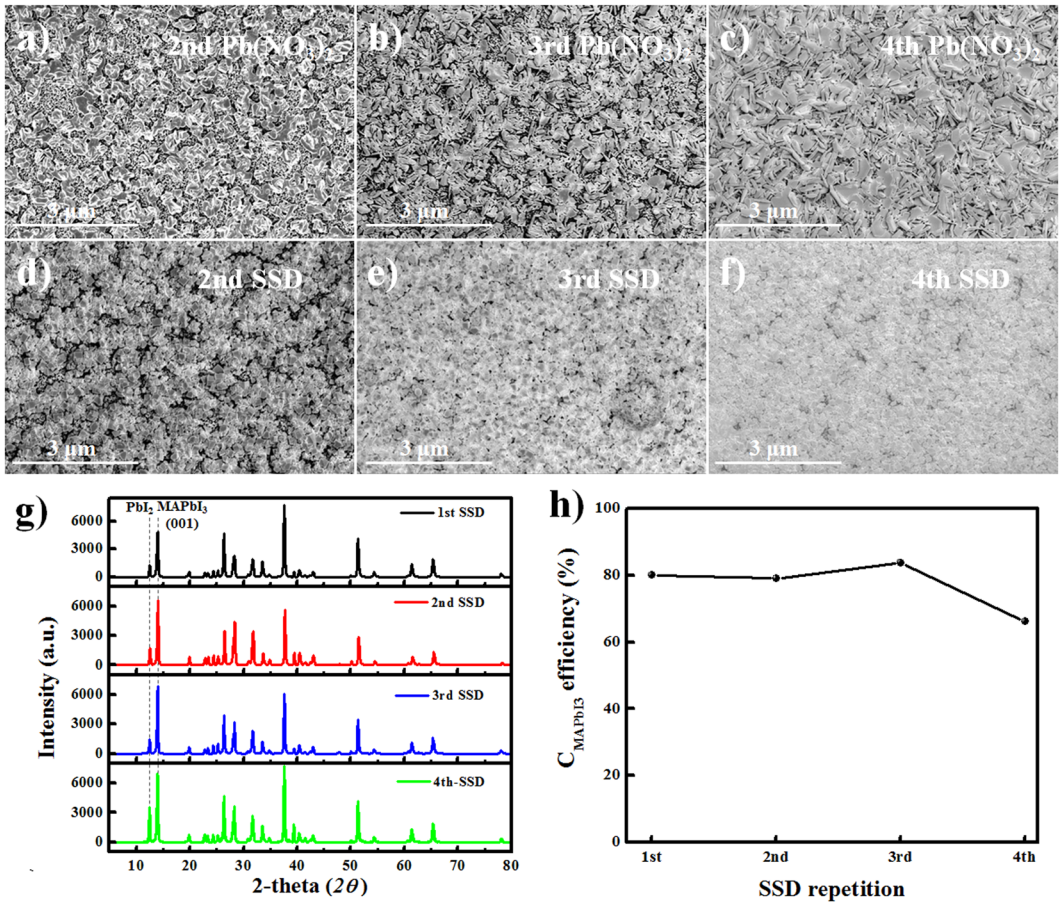

Figure 6. (**a**–**f**) The SEM surface morphologies of the $MAPbI_3$ perovskite layers fabricated using the conventional SSD process through (**a**–**c**) ionic layer adsorption of $Pb(NO_3)_2$ from aqueous solution followed by (**d**–**f**) the reaction in MAI solution. (**g**) The XDR patterns of the $MAPbI_3$ perovskite layers and (**h**) the correlation between the perovskite conversion and SSD repetition time.

the efficiency of the HTM was improved with doping additives such as 4-tert-butylpyridine (t-BPy) and lithium bis(trifluoromethanesulfonyl) imide (Li-TFSI).

The optimization of the device performance is shown in Figs S5–9. As shown in Fig. 7a, the optimized PrSC devices exhibited the most efficient PCE (maximum/average) of 12.41/11.58% with a short-circuit current density (J_{sc}) of 21.53 mA/cm^{-2}, an open-circuit voltage (V_{oc}) of 0.93 V, and a fill factor (*FF*) of 0.62. The PCEs of the devices based on $MAPbI_3$ perovskite layers fabricated with different numbers of SSD cycles were not as high. One SSD cycle gave PCEs (maximum/average) of 8.73/7.01% with $J_{sc} = 14.66\,mA{\cdot}cm^{-2}$, $V_{oc} = 0.98$ V, and $FF = 0.61$; two cycles gave PCEs of 9.07/8.05% with $J_{sc} = 15.00\,mA{\cdot}cm^{-2}$, $V_{oc} = 0.96$ V, and $FF = 0.63$; and four cycles gave PCEs of 10.16/8.05% with $J_{sc} = 17.00\,mA{\cdot}cm^{-2}$, $V_{oc} = 0.98$ V, and $FF = 0.61$. These results can be explained by the improved surface coverage and crystallinity of the films formed from sequential deposition with 3 SSD and 3 SSIER cycles, as shown in Fig. 4. In addition, the optimized PrSCs exhibited much higher performances than those based on non-halide precursors such as $Pb(OAc)_2$ and $Pb(ClO_4)_2$ (Fig. S10).

Meanwhile, the typical n-i-p PrSCs fabricated with the m-TiO_2 electrode often show hysteretic *J-V* behavior depending on the scan direction (reverse or forward) due to differing charge extraction or transportation rates of holes and electrons separated from excitons[10]. Fig. 7b shows the hysteresis of the *J-V* curves in both scan directions under AM 1.5 irradiation (100 mW·cm^{-1}) for the optimized PrSC. The hysteresis behaviors of the PrSCs are shown in Fig. 7b and are summarized in Fig. S11 and Table S1. Most of PrSCs exhibited negligible differences in J_{sc} and V_{oc} values in both directions, but the *FF* values were significantly reduced in the forward direction. Nonetheless, the average of the PCE values obtained in both directions was approximately 6% lower than the PCE value in the reverse direction, showing good external quantum efficiency (EQEs) in the light absorption region (Fig. S12).

Large surface area perovskite films. Next, we characterized the cross-sectional morphology of the optimized PrSC device. Figure 8a shows the SEM image of a cross-section of the PrSC device fabricated using 3 SSD and 3 SSIER cycles with a final incubation for 600 s in the MAI solution. A ~100 nm thin section was prepared using the focused ion beam (FIB) technique to investigate the vertically formed morphologies and interfacial heterojunctions between the MAPbI3 perovskite, ZnO, and m-TiO_2/c-TiO_2 electrodes.

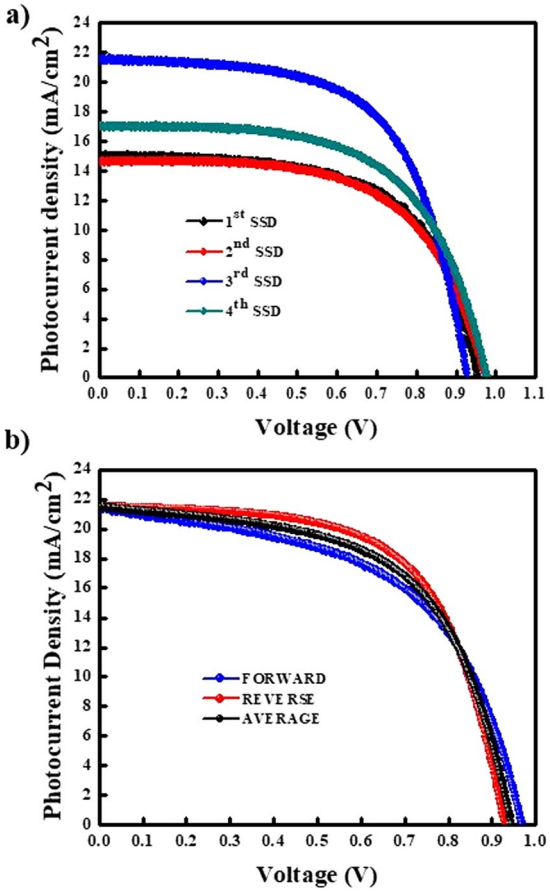

Figure 7. (**a**) Current-voltage (*J-V*) curves under AM 1.5 irradiation (100 mW·cm^{-1}) for PrSCs based on $MAPbI_3$ perovskite layers fabricated by a designated number of SSD repetitions followed by 3 SSIER cycles, with a final incubation for 600 s in the MAI solution. (**b**) The hysteresis behavior of the PrSCs fabricated under the optimized conditions (3 SSD and 3 SSIER processes, 600 s MAI incubation).

As shown in Fig. 8a, the $MAPbI_3$ perovskite layer was well organized between the spiro-MeOTAD HTM and ZnO/m-TiO_2/c-TiO_2/FTO substrate without interfacial dead spaces. However, the film was non-uniform and thin with a thickness of approximately 250 nm, in contrast to the high efficiency PrSCs reported previously. Herein we prepared a large area perovskite film using a sequential dip-coating deposition approach with a non-halide lead precursor in aqueous solution to facilitate a green and low-cost manufacturing process. The photograph in Fig. 8b shows the $MAPbI_3$ perovskite films fabricated by a sequential SSD and SSIER deposition approach on large area glass substrates. To demonstrate a large area $MAPbI_3$ perovskite film, we prepared a thin ZnO layer on a bare FTO substrate of 780 cm^2 (30 cm × 26 cm, width × height) using the dip-coating method. Then, the $MAPbI_3$ perovskite films were deposited with the sequential SSD and SSIER approach. Even though this large area $MAPbI_3$ perovskite film was non-uniform due to the uneven surface morphology of the ZnO under layer, we successfully realized a large area perovskite film using the sequential dip-coating deposition approach with a non-halide lead precursor in an aqueous solution. This represents significant progress towards environmentally benign and low-cost manufacturing processes for large area PrSCs.

Conclusion

We have demonstrated an efficient approach for preparing large area $MAPbI_3$ perovskite films using sequential dip-coating deposition with ionic layer adsorption of $Pb(NO_3)_2$ in aqueous solvent followed by reaction with MAI. This represents significant progress toward an environmentally benign and low-cost manufacturing processes for large area PrSCs. Notably, the ZnO interfacial layer induced significant adsorption of $Pb(NO_3)_2$ from aqueous solution within a very short period. A new SSIER approach was developed to prevent the decomposition of $MAPbI_3$ perovskite structures formed from $Pb(NO_3)_2$ and MAI, which was rapidly followed by ion-exchange reactions with unreacted $Pb(NO_3)_2$ even in the solid-state. The method developed herein afforded superior stability, surface coverage, and crystallinity of MAPbI3 perovskite films compared to those prepared without the SSIER process. In addition, the introduction of the SSD process to the SSIER approach led to more complete surface coverage with the $MAPbI_3$ perovskite films affording superior morphology, stability, and crystallinity. The PrSCs based on these sequential depositions of the $MAPbI_3$ perovskite layer using aqueous $Pb(NO_3)_2$ solution exhibited excellent PCEs of 12.41%, which is comparable to films fabricated from spin-casting of halide or non-halide lead

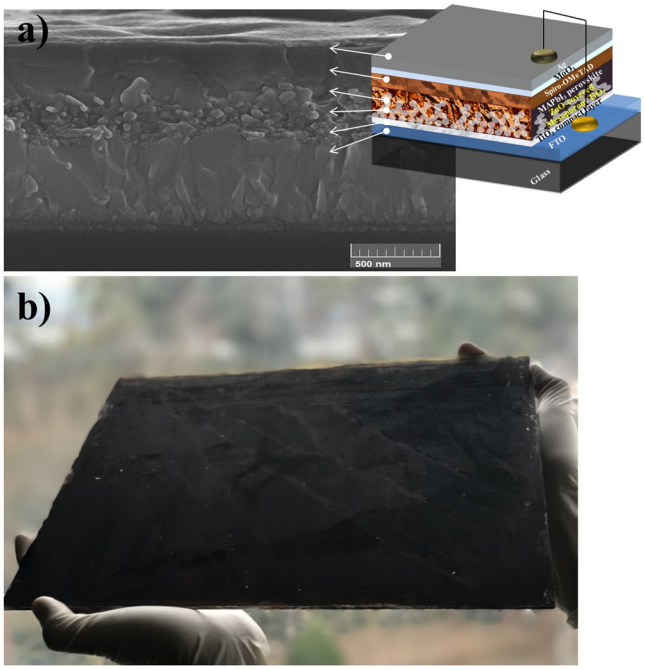

Figure 8. (**a**) The SEM image of a cross-section of the PrSC device fabricated using 3 SSDs and 3 SSIER repetitions with a final incubation of 600 s in the MAI solution. (**b**) Photograph of a large area $MAPbI_3$ perovskite film fabricated by sequential SSD and SSIER deposition on large area glass substrate of 780 cm^2 (30 cm (width) × 26 cm (height)).

precursors. The results of this study lay the groundwork for the development of environmentally benign and low-cost manufacturing of high efficiency and large area PrSCs.

Methods

Materials. The $MAPbI_3$ was prepared according to a method reported previously[1]. All solvents were purchased from Sigma-Aldrich, TCI, and Alfa Aesar and were purified using appropriate methods. The $MAPbI_3$ precursor solution was prepared under a nitrogen atmosphere. Spiro-OMeTAD was obtained from Solaronix.

Fabrication of $MAPbI_3$ perovskite films. For the fabrication of $MAPbI_3$ perovskite film, we applied a novel SSIER approach. A metal oxide-coated FTO substrates was first dipped into a 0.1 M solution of $Pb(NO_3)_2$ (Sigma-Aldrich, 99.9%) dissolved in ethanol/water (2:1, v/v) for approximately 30 s. The substrate was washed with deionized (DI) water and ethanol and then annealed at 120 °C for 10 min, resulting in the formation of a transparent film. The substrate was dipped into a 0.1 M MAI solution in isopropanol (Sigma-Aldrich, 99.5%), for 30 s, washed with chloroform and diethyl ether (Sigma-Aldrich, >96%), and annealed at 80 °C for 10 min. The above procedure represents a single SSIER cycle. After the desired number of SSIER repetitions, the prepared films were exposed for 600 s to the MAI solution, followed by annealing at 80 °C for 10 min. In addition to the SSIER process, the SSD process was performed. In the first cycle of the SSD process, the metal oxide-coated FTO substrates were dipped into a 0.1 M solution of $Pb(NO_3)_2$ dissolved in ethanol/water (2:1, v/v) for approximately 30 s, washed using pure water and ethanol, and annealed at 120 °C for 10 min. The $Pb(NO_3)_2$ layer-coated substrate was then dipped into the MAI solution for 30 s followed by annealing at 80 °C for 10 min. The above procedure represents a single SSD cycle. After the designated number of SSD repetitions, the SSIER process was subsequently performed to provide an improved $MAPbI_3$ perovskite film.

PrSC device fabrication. A clean FTO was UVO treated for 10 min. The TiO_2 blocking layer (bl-TiO_2) was spin coated on a FTO glass substrate with a titanium(IV) diisopropoxide bis(acetylacetonate) solution diluted in butanol (1:10, v/v) at 700 rpm for 8 sec, 1000 rpm for 10 sec and 2000 rpm for 40 sec followed by dryig at 125 °C for 5 min. Mesoporous titanium oxide (mp-TiO_2) layer was spin coated on the bl-TiO_2 with 1.2 g of TiO_2 nanoparticles (40 nm size from ENB Korea) diluted in 10 ml of anhydrous ethanol solution at a speed of 2000 rpm for 20 sec and finally annealed at 550 °C for 1 hr and the UVO treated for 15 min. The ZnO sol-gel was synthesized by reacting zinc acetate dihydrate (1.6 g, Sigma Aldrich), ethanolamine (0.5 g, Sigma Aldrich) and 2-methoxy-ethanol (10 ml, Sigma Aldrich) and stirr for 4 hrs at room temperature and spin coated over the mp-TiO_2 at 5000 rpm for 40 sec and finally annealed at 300 °C for 1 hr[33]. $MAPbI_3$ layers were fabricated according to the method described above. The Spiro-OMeTAD HTM was deposited via spin-coating at 3000 rpm for 30 s. The solution was prepared by mixing 29 mg of Spiro-OMeTAD, 7 μL of 170 mg/ml Li-TFSI in acetonitrile, and 11 μL of 4-tBPy. Finally, device fabrication was completed by thermal evaporation of the thin MoO_3 layer and thick Ag layer on top of the HTM film under reduced pressure (less than 10^{-6} Torr).

Measurements and Instrument. The absorption spectra were recorded on a PerkinElmer Lambda 2S ultraviolet (UV)-visible spectrometer. The surface morphologies were investigated using a field emission scanning electron microscope (FESEM, Nova Nano-SEM 450, FEI, Netherlands). The perovskite crystallinities of the MAPbI3 layers were determined using X-ray diffraction (XRD, D/Max2500 V/PC, Rigaku Corp, Japan). The solar cell efficiencies were characterized under simulated 100 $mW \cdot cm^{-1}$ AM 1.5 G irradiation from a Xe arc lamp with an AM 1.5 global filter. The simulator irradiance was characterized using a calibrated spectrometer; the illumination intensity was set using a silicon diode with an integrated KG1 optical filter certified by the National Renewable Energy Laboratory (NREL). The spectral mismatch factors were less than 5% for each device. The short circuit currents were also within 5% of the values calculated using the integrated EQE spectra and the solar spectrum. The applied potential and cell currents were measured using a Keithley 2400 model digital source meter. The *J-V* curves were measured at a voltage settling time of 100 ms. The EQEs were measured by under-filling the device area using a reflective microscope objective to focus the light output from a 75 W Xe lamp, monochromator, and optical chopper. The photocurrent was measured using a lock-in amplifier and the absolute photon flux was determined using a calibrated silicon photodiode and was recorded for 5 s per point (80 points) from 350 to 900 nm. In the *J-V* curves hysteresis tests, the "forward" scan means to measure the sweeping voltage from the short circuit to forward bias, whereas a "backward" scan means to sweep in the opposite direction. To explore the active area of device and avoid scattering effects from the edges, a non-reflective metal plate mask with an aperture of 4.5 mm^2 was used for the solar cells.

References

1. Saliba, M. *et al*. Cesium-containing triple cation perovskite solar cells: improved stability, reproducibility and high efficiency. *Energy Environ. Sci.* **9**, 1989–1997 (2016).
2. Heo, J. H. *et al*. Efficient inorganic–organic hybrid heterojunction solar cells containing perovskite compound and polymeric hole conductors. *Nat. Photon.* **7**, 486–491 (2013).
3. Etgar, L. *et al*. Mesoscopic $CH_3NH_3PbI_3/TiO_2$ heterojunction solar cells. *J. Am. Chem. Soc.* **134**, 17396–17399 (2012).
4. Lee, M. M. *et al*. Efficient Hybrid Solar Cells Based on Meso-Superstructured Organometal Halide Perovskites. *Science.* **338**, 643–647 (2012).
5. Noh, J. J. *et al*. Chemical Management for Colorful, Efficient, and Stable Inorganic–Organic Hybrid Nanostructured Solar Cells. *Nano Letter.* **13**, 1764–1769 (2013).
6. Abrusci, A. *et al*. High-Performance Perovskite-Polymer Hybrid Solar Cells via Electronic Coupling with Fullerene Monolayers. *Nano Letter.* **13**, 3124–3128 (2013).
7. Malinkiewca, O. *et al*. Perovskite solar cells employing organic charge-transport layers. *Nat. Photon.* **8**, 128–132 (2014).
8. Kim, H. S. *et al*. Lead Iodide Perovskite Sensitized All-Solid-State Submicron Thin Film Mesoscopic Solar Cell with Efficiency Exceeding 9%. *Sci. Rep.* **2**, 591 (2012).
9. Kojima, A. *et al*. Organometal Halide Perovskites as Visible-Light Sensitizers for Photovoltaic Cells. *J. Am. Chem. Soc.* **131**, 6050–6051 (2009).
10. Meng, L. *et al*. Recent Advances in the Inverted Planar Structure of Perovskite Solar Cells. *Acc. Chem. Res.* **49**, 155–165 (2016).
11. Burschka, J. *et al*. Sequential deposition as a route to high-performance perovskite-sensitized solar cells. *Nature* **499**, 316 (2013).
12. Liu, M. *et al*. Efficient planar heterojunction perovskite solar cells by vapour deposition. *Nature.* **501**, 395 (2013).
13. Zhang, W. *et al*. Ultrasmooth organic–inorganic perovskite thin-film formation and crystallization for efficient planar heterojunction solar cells. *Nat. Commun.* **6**, 6142 (2015).
14. Aldibaja, F. K. *et al*. Effect of different lead precursors on perovskite solar cell performance and stability. *J. Mater. Chem. A.* **3**, 9194–9200 (2015).
15. Xiao, Z. *et al*. Large fill-factor bilayer iodine perovskite solar cells fabricated by a low-temperature solution-process. *Energy Environ. Sci.* **7**, 2619–2623 (2014).
16. Hsu, H. *et al*. Two-step thermal annealing improves the morphology of spin-coated films for highly efficient perovskite hybrid photovoltaics. *Nanoscale.* **6**, 10281–10288 (2014).
17. Sun, S. *et al*. Benefits of very thin PCBM and LiF layers for solution-processed p–i–n perovskite solar cells. *Energy Environ. Sci.* **7**, 399–407 (2014).
18. Xiao, M. *et al*. Flexible and Semitransparent Organolead Triiodide Perovskite Network Photodetector Arrays with High Stability. *Angew. Chem, Int. Ed.* **53**, 10056–10061 (2014).
19. Ahn, N. *et al*. Highly Reproducible Perovskite Solar Cells with Average Efficiency of 18.3% and Best Efficiency of 19.7% Fabricated via Lewis Base Adduct of Lead(II) Iodide. *J. Am. Chem. Soc.* **137**, 8696–8699 (2015).
20. Lee, J. W. *et al*. Lewis Acid–Base Adduct Approach for High Efficiency Perovskite Solar Cells. *Acc. Chem. Res.* **49**, 311–319 (2016).
21. Liang, P. *et al*. Additive enhanced crystallization of solution-processed perovskite for highly efficient planar-heterojunction solar cells. *Adv. Mater.* **26**, 3748–3754 (2014).
22. Chueh, C. *et al*. The roles of alkyl halide additives in enhancing perovskite solar cell performance. *J. Mater. Chem. A.* **3**, 9058–9062 (2015).
23. Song, S. *et al*. Additive to regulate the perovskite crystal film growth in planar heterojunction solar cells. *Chen, Appl. Phys. Lett.* **106**, 033901 (2015).
24. Colella, S. *et al*. $MAPbI_{3-x}Cl_x$ Mixed Halide Perovskite for Hybrid Solar Cells: The Role of Chloride as Dopant on the Transport and Structural Properties. *Chem. Mater.* **25**, 4613–4618 (2013).
25. Kim, H. *et al*. Large fill-factor bilayer iodine perovskite solar cells fabricated by a low-temperature solution-process. *Chem. Asian J.* **11**, 2393–2399 (2016).
26. Jeng, J. Y. *et al*. CH3NH3PbI3 Perovskite/Fullerene Planar-Heterojunction Hybrid Solar Cells. *Adv. Mater.* **25**, 3727–3732 (2013).
27. Hsieh, T. Y. *et al*. $CH_3NH_3PbI_3$ Perovskite/Fullerene Planar-Heterojunction Hybrid Solar Cells. *Chem. Commun.* **51**, 13294–13297 (2015).
28. Li, H. *et al*. Reaction mechanism of a PbS-on-ZnO heterostructure and enhanced photovoltaic diode performance with an interface-modulated heterojunction energy band structure. *Phys. Chem. Chem. Phys.* **18**, 4144–4153 (2016).
29. Li, H. *et al*. Tunable growth of PbS quantum dot–ZnO heterostructure and mechanism analysis. *CrystEngComm.* **17**, 4722–4728 (2015).
30. Nicolau, Y. *et al*. F. Solution deposition of thin solid compound films by a successive ionic-layer adsorption and reaction process. *Appl. Surf. Sci.* **22/23**, 1061–1074 (1985).
31. Snaith, H. J. *et al*. Anomalous Hysteresis in Perovskite Solar Cells. *J. Phys. Chem. Lett.* **5**, 1511–1515 (2014).
32. Unger, E. L. *et al*. Hysteresis and transient behavior in current-voltage measurements of hybrid-perovskite absorber solar cells. *Energy Environ. Sci.* **7**, 3690–3698 (2014).
33. Sun, Y. *et al*. Inverted polymer solar cells integrated with a low-temperature-annealed sol-gel-derived ZnO Film as an electron transport layer. *Adv. Mater.* **23**, 1679–1683 (2011).

Acknowledgements
This work was financially supported by Basic Science Research Program through the National Research Foundation of Korea (NRF-2015R1D1A1A01057125).

Author Contributions
M.A. performed all experiments of this work. J.K.L. provided guidance and feedback throughout the study and edited and reviewed the manuscript simultaneously.

Additional Information
Supplementary information accompanies this paper at https://doi.org/10.1038/s41598-018-20296-2.

Competing Interests: The authors declare that they have no competing interests.

Publisher's note: Springer Nature remains neutral with regard to jurisdictional claims in published maps and institutional affiliations.